COMMUNICATIONS MATERIALS

ARTICLE

https://doi.org/10.1038/s43246-020-0027-0 OPEN

Strain-induced structure and oxygen transport interactions in epitaxial $La_{0.6}Sr_{0.4}CoO_{3-\delta}$ thin films

Yurii P. Ivanov[1,2,3]✉, Markus Kubicek[4], Matthäus Siebenhofer[4], Alexander Viernstein[4], Herbert Hutter[4], Jürgen Fleig[4], Andrey Chuvilin[5,6] & Zaoli Zhang[1]

The possibility to control oxygen transport in one of the most promising solid oxide fuel cell cathode materials, $La_{0.6}Sr_{0.4}CoO_{3-\delta}$, by controlling lattice strain raises questions regarding the contribution of atomic scale effects. Here, high-resolution transmission electron microscopy revealed the different atomic structures in $La_{0.6}Sr_{0.4}CoO_{3-\delta}$ thin films grown under tensile and compressive strain conditions. The atomic structure of the tensile-strained film indicated significant local concentration of the oxygen vacancies, with the average value of the oxygen non-stoichiometry being much larger than for the compressive-strained film. In addition to the vacancy concentration differences that are measured by isotope exchange depth profiling, significant vacancy ordering was found in tensile-strained films. This understanding might be useful for tuning the atomic structure of $La_{0.6}Sr_{0.4}CoO_{3-\delta}$ thin films to optimize cathode performance.

[1] Erich Schmid Institute of Materials Science, Austrian Academy of Sciences, Jahnstraße 12, A-8700 Leoben, Austria. [2] Department of Materials Science & Metallurgy, University of Cambridge, Cambridge CB3 0FS, UK. [3] School of Natural Sciences, Far Eastern Federal University, 690950 Vladivostok, Russia. [4] Institute of Chemical Technologies and Analytics, Vienna University of Technology, Getreidemarkt 9, A-1060 Vienna, Austria. [5] CIC nanoGUNE BRTA, Avenida de Tolosa 76, 20018 San Sebastian, Spain. [6] IKERBASQUE, Basque Foundation for Science, Maria Diaz de Haro 3, 48013 Bilbao, Spain. ✉email: ivanov.yup@gmail.com

Mixed ionic and electronic conducting (MIEC) oxides constitute an important materials class for solid oxide fuel cells (SOFCs), sensors, or permeation membranes. Mixed conducting $La_{0.6}Sr_{0.4}CoO_{3-\delta}$ (LSCO), for example, is among the most promising SOFC cathode materials, particularly for reduced operation temperature[1–3]. The latter requires cathode materials with fast oxygen exchange and diffusion kinetics to keep the related polarization resistances acceptably small. In recent years, efforts for improvement were made not only by optimizing the compositions of MIEC oxides, but also by modifying existing materials, for example by controlling their microstructure[4–6], dislocation density[7,8], or lattice strain[9–11]. Among those, a control of the lattice strain showed very promising results, demonstrating dramatic differences in oxygen transport between in-plane tensile and compressive-strained samples. Thus, in-plane tensile-strained epitaxial $La_{0.8}Sr_{0.2}CoO_{3-\delta}$ showed a strong enhancement of the oxygen diffusion coefficient compared to a compressively strained $La_{0.8}Sr_{0.2}CoO_{3-\delta}$ epitaxial layer[9]. Additionally, also an activation effect on the surface exchange coefficient is observed[9].

These differences are determined by at least two possible strain effects convoluted in the isotope exchange data: (i) a change in the migration barrier for the mobile oxygen species in certain directions and (ii) a strain-induced change of the oxygen vacancy formation enthalpy resulting in a higher concentration of vacancies. The latter effect may also explain the measured higher surface exchange coefficient in tracer experiments on in-plane tensile-strained LSCO. High enough concentration of the oxygen vacancies in perovskites might result in the doubling of the unit cell to form so-called Brownmillerite phase[12]. Such superstructure results in periodic bright and dark stripes on the high resolution scanning transmission electron microscopy (STEM) images[13–15] and typically it is not observed in Sr-doped LSCO at Sr substitution below 50%[16–20]. Recent computational studies on related $LaCoO_3$[21] also revealed that changes of the lattice strain can strongly influence the mobility of oxygen in certain directions. Different possible effects of global vs. local strain fields[2,22,23] (e.g., around dislocations) or different effects of the same strain in different materials need to be considered. An experimental deconvolution of individual local strain effects on the oxygen exchange kinetics with combined in-plane and across-plane diffusion experiments has not been attempted so far to the best of the authors' knowledge.

Here we aim to investigate the local atomic structure in epitaxial films macroscopically strained (tensile/compressive) due to the corresponding mismatch with the substrate and link it to the oxygen diffusion kinetics. We combine high-resolution transmission electron microscopy (HRTEM) methods with isotope tracer experiments probing the in-plane diffusion of oxygen. Our observations reveal the epitaxial growth of LSCO on $LaAlO_3$ (LAO) substrate with out-of-plane tensile stress of about 3% in respect to the substrate, and the pronounced oxygen vacancies ordering in Brownmillerite phase of LSCO growing on the $SrTiO_3$ (STO) substrate with both in-plane and out-of-plane average lattice parameters to be similar to the STO substrate (see schematics in Fig. 1). Local crystal lattice changes observed by TEM in combination with analysis of the oxygen vacancy concentration and the diffusion coefficient measurements shed new light on the relationship of local crystal structure and composition with macroscopic electrochemical properties.

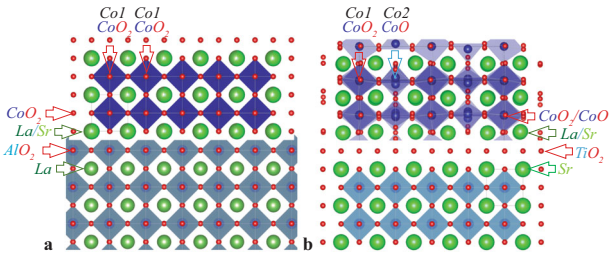

Fig. 1 Schematics of the oxygen vacancy ordering depending on the substrate used for growing LSCO thin films. The cubic perovskite phase of LSCO (**a**) transforms to its Brownmillerite phase (**b**) (characterized by oxygen vacancies ordering due to the alternating octahedra (Co1 O_6) and tetrahedra (Co2 O_4) coordination of Co ions) by strain engineering.

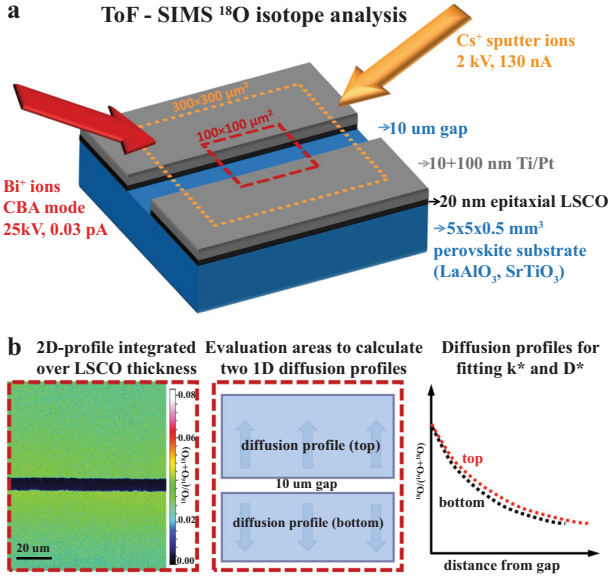

Fig. 2 Schematic of the in-plane isotope experiments. An LSCO thin film is epitaxially grown on a perovskite substrate and a capping layer of 10 + 100 nm Ti + Pt is sputtered on top. Using photolithography and Ar^+ ion beam etching, a 10 μm wide gap is opened in all layers and ^{18}O isotope exchange is performed via the exposed LSCO surface at both sides of the gap (**a**). By ToF-SIMS both sides of the gap are analyzed, and the collected 3D isotope distribution data is converted into two 1D in-plane diffusion profiles as shown schematically in **b**.

Results and discussion

ToF-SIMS in-plane isotope profiles. ^{18}O oxygen profiles were measured on epitaxial LSCO thin films grown either on LAO with in-plane compressive strain or on STO with in-plane tensile strain. The temperature range 680–780 °C was investigated, and isotope exchange experiments with samples of both LSCO strains were always performed simultaneously. Using time-of-flight-secondary ion mass spectrometry (ToF-SIMS), the three-dimensional (3D) distribution of ^{18}O and ^{16}O was measured. Conversion of the 3D information to one-dimensional (1D) diffusion profiles was performed as depicted in Fig. 2. First the isotope concentration $^{18}O/(^{16}O + ^{18}O)$ was integrated over the thickness of the LSCO layer yielding a two-dimensional (2D) isotope distribution image (shown in Fig. 2 and as an insert in Fig. 3a, b). From this image the data from the free etched gap were discarded and on both sides of the gap, 1D isotope profiles (see Figs. 2 and 3) were calculated via integration in the respective direction perpendicular to the gap. Fitting of k^* and D^* was done by linear least squares method using an analytical solution to Fick's diffusion law for a constant outside concentration[24].

In Fig. 3, typical ^{18}O isotope profiles of LSCO with in-plane compressive and in-plane tensile strain are shown with their respective fit functions used to evaluate the oxygen exchange

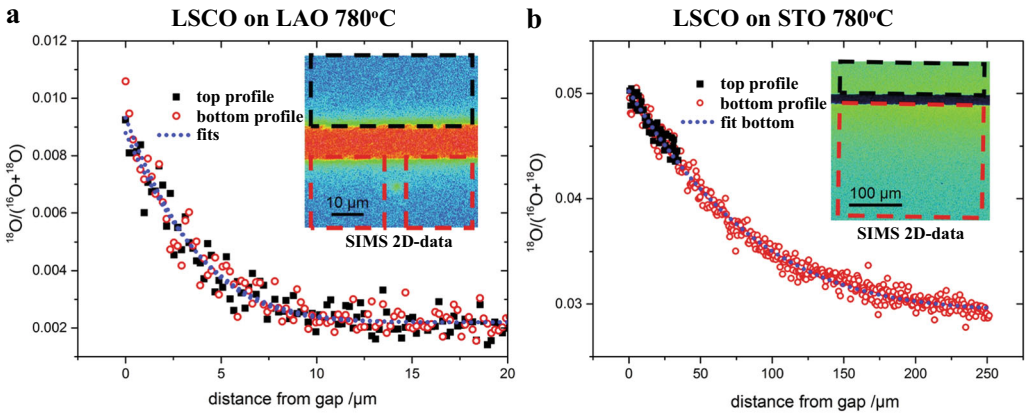

Fig. 3 Exemplary ^{18}O in-plane diffusion profiles of epitaxial LSCO thin films. LSCO is grown with compressive strain on LAO (**a**) and with tensile strain on STO (**b**). The integration area to generate 1D profiles was adapted where pinholes or defects were present (see the bottom part of the inlay graphic (**a**)). In the case of LSCO/STO at the highest temperature, where very long diffusion lengths were observed, an asymmetric alignment of the gap was chosen to allow for measuring a longer diffusion profile in one direction (see (**b**)).

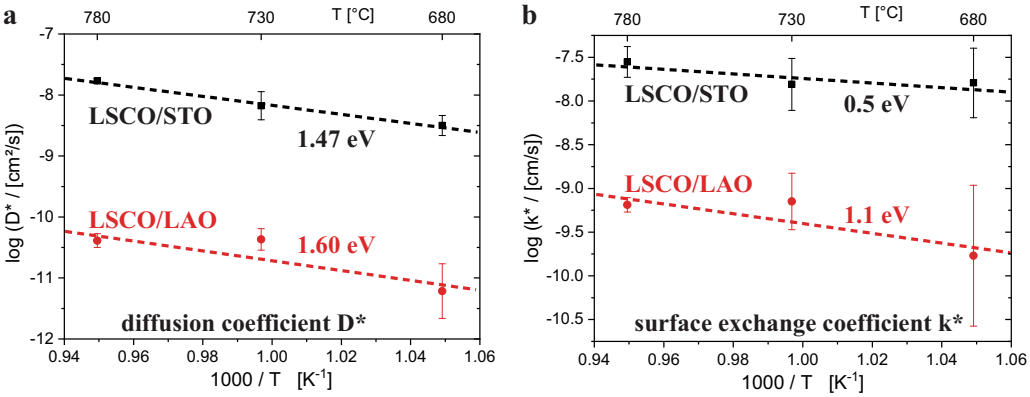

Fig. 4 The results of the in-plane isotope exchange measurements. Evaluation of the tracer surface exchange parameter k^* (**a**) and the tracer diffusion coefficient D^* (**b**) for three different temperatures, 680, 730, and 780 °C. Error bars were calculated from at least four individual 1D diffusion profiles measured for each temperature and substrate. The respective fitting curves and activation energies are plotted, assuming Arrhenius-type behavior. The error bars show the standard deviation for the measurements.

coefficient (k^*) and diffusion coefficient (D^*). The inlays show the 2D distribution of the ^{18}O and the integration areas used to calculate the 1D profiles. In a few analyzed areas, inhomogeneities or pinholes were visible in the 2D images, such as in Fig. 3a (bottom and center), those areas were excluded in further analysis (see red dashed boxes). In general, diffusion profiles showed excellent agreement with their respective fit function. Additionally, the values of the tracer diffusion coefficient D^* from different measurement areas were very reproducible as can be seen from the small error bars from combining all measurements in Fig. 4a. A larger scatter was observed for the tracer surface exchange coefficient k^* as shown in Fig. 4b. Here we expect the very small incorporation zone (only 20 nm broad) to be the reason behind the observed variation. Additionally, the free LSCO surface was created by ion beam etching. The high energy ions can certainly damage the surface upon impact, which explains both a lower surface exchange compared to literature[25] and a large scatter. Additionally, in the investigated temperature range, also Sr segregation[26] at the surface may reduce the surface exchange. However, the determination of the diffusion coefficient is not hampered by these surface effects as the profiles propagate over several micrometers, much deeper than the few nanometers deep zone where LSCO may be altered by ion beam damage or Sr segregation.

Over the measured temperature range, we can clearly confirm for both parameters D^* and k^* that the tensile strain leads to faster diffusion and oxygen exchange. This difference due to strain is more pronounced in the diffusion coefficient D^* of LSCO. Here, a factor ~300 difference was found throughout the investigated temperature range with only minor differences in temperature dependence manifested in similar activation energies (1.47 and 1.60 eV, respectively). The observed difference in k^* for the two strain states was about 1–2 orders of magnitude in the investigated temperature interval. As discussed above, k^* values were in general smaller than literature which we attribute to adverse effects from ion irradiation. Consequently, the differences may also be influenced by different relaxation of the free-cut surfaces or similar and the focus is laid on the diffusion characteristics.

Two strain-dependent parameters may affect the diffusion coefficient: the oxygen vacancy concentration and the vacancy mobility characterized by the migration enthalpy. In an earlier study[9], the across-plane diffusion in LSCO was investigated via isotope exchange depth profiling on equivalent 20 nm $La_{0.8}Sr_{0.2}CoO_{3-\delta}$ (LSCO82) and $La_{0.6}Sr_{0.4}CoO_{3-\delta}$ (LSCO64) thin films grown epitaxially on LAO and STO substrates. There, for LSCO82 the same clear trend of tensile strain enhancing diffusion and surface exchange was observed. For LSCO64 it was not

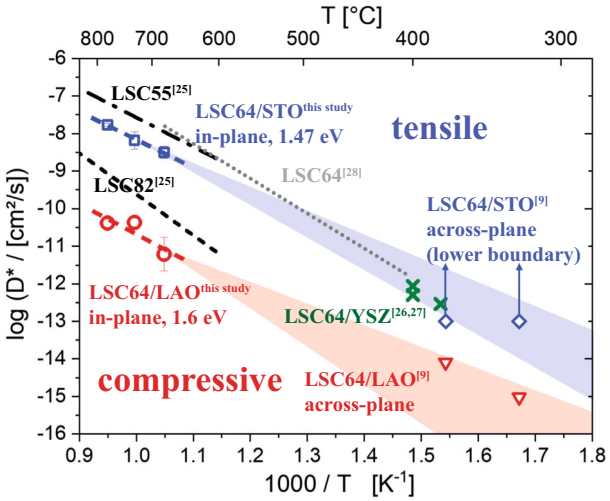

Fig. 5 Arrhenius-type plot of the tracer diffusion coefficient *D measured for different LSCO types.** Blue: tensile epitaxial LSCO64 thin films: this study and ref. [9]. Red: compressive epitaxial LSCO64 thin films: this study and ref. [9]. Green: columnar polycrystalline LSCO64 thin films[26, 40], black-gray: bulk LSCO[41]. The error bars show the standard deviation for the measurements.

possible to find suitable conditions for exactly determining the high D^* of the tensile strain state[9]. The reason is that incorporation is surface limited and our investigated diffusion length is small due to the 20 nm thin films. Therefore, when performing the experiment at the low temperatures/times necessary for achieving a diffusion length in the order of the film thickness, virtually no ^{18}O is incorporated via the surface. For higher temperatures/times where detectable amounts ^{18}O are incorporated, a lower boundary for D^* could be determined, see the arrows in Fig. 5. For tensile LSCO/STO, only a lower boundary for D^* could be given due to an almost flat diffusion profile, see the arrows in Fig. 5. At 325 °C at least 2 orders of magnitude difference in D^* was observed between LSCO64 on LAO ($D^* = 9.5 \times 10^{-16}$ cm^2/s) and STO ($D^* > 10^{-13}$ cm^2/s).

In Fig. 5, an overview of tracer diffusion coefficients measured on LSCO is shown. Three colors are used for different microstructures and strains: (i) blue for tensile LSCO64 thin films on STO, (ii) red for compressive LSCO64 thin films on LAO, (iii) green for columnar/polycrystalline LSCO64 thin films on YSZ, and (iv) black/gray for bulk LSCO. We now compare (i) and (ii) for the two diffusion directions (in-plane at high T, and across-plane at low T) by extrapolating the in-plane data to low temperatures (transparent broad lines in Fig. 5). It is clearly visible that there is always an enhanced diffusion for tensile strain, no matter which direction diffusion is measured. From the fact that both measurement types are acceptably explainable by that extrapolation, we can conclude that from three possible strain effects: changed vacancy concentration, an overall change in migration barrier due to strain, and a direction-specific change due to elongation/compression, we can exclude the last to be impactful. Comparison of the strained epitaxial thin films (i and ii) to polycrystalline thin films (iii) reveals a smaller enhancement for tensile strain and a stronger reduction for compressive strain. However, the absence (i and ii) and presence (iii) of the grain boundaries may also contribute to this effect.

Comparison of thin film samples to bulk LSCO (iv) shows that even for the tensile strain state, the high bulk diffusion coefficients are not fully reached, despite higher vacancy concentrations are present in tensile thin films. Consequently, the mobility of vacancies has to be reduced in tensile thin films, which is not surprising as strong defect interactions and vacancy ordering is observed. Similar observations of higher vacancy concentration but lower mobility were reported in the literature, e.g., in the vicinity of dislocations for $SrTiO_3$[23,27], or for acceptor doped ceria[28].

Structural study. Figure 6 shows X-ray diffraction (XRD) in Bragg–Brentano geometry and X-ray reciprocal space mapping (RSM) on LSCO thin films deposited on LAO and STO substrates. Only {00l} type diffraction peak of LSCO is observed. The good quality of the 20 nm epitaxial thin films is shown by the visible Kiessig fringes on the inserts of Fig. 6a, b. From RMS study the thin film peaks are broader for LSCO/LAO film.

To investigate the local structural reasons behind the observed difference of the D^* and k^*, we performed a systematic TEM study of LCSO films grown on the LAO and STO substrates. Figure 7 shows LSCO film deposited on the LAO substrate. The very good epitaxial quality of the film is clearly visible for the whole film thickness, Fig. 7a. High angle annual dark field (HAADF) STEM images revealed non-homogeneous contrast of the cation columns due to the mixed A-site cation occupation ($La_{0.6}$, $Sr_{0.4}$: Z(La) = 57, Z(Sr) = 38).

To evaluate the lattice parameter of the film and substrate, we used custom Digital Micrograph Scripts[29] to perform Geometrical Phase Analysis (GPA) on HAADF images. Figure 7b, c shows the results of GPA for two orthogonal lattice plane systems (001) and (100), which are respectively parallel and normal to the LAO substrate plane. The in-plane lattice parameter of the LSCO accommodates almost perfectly to the LAO substrate. The bulk values of lattice constants are 0.381 nm for LAO and 0.387 nm for LSCO. The value of the in-plane parameter $d_{(100)\perp}$ of the LSCO layer extracted from the HAADF images is close to the one of bulk LAO—$0.3815 \pm 2 \times 10^{-5}$ nm. Thus, the LSCO film experiences a compressive in-plane strain, which is as expected due to the small mismatch of the lattice parameter with the substrate. In out-of-plane direction GPA measures a global expansion to an average value of $d_{(001)\parallel} = 0.395$ nm, Fig. 7c. In addition, this parameter shows a regular periodic modulation with the period of two unit cells, Fig. 7d, which may be attributed to the oxygen vacancy ordering[12,30–33]. From the GPA measurements we calculate the distribution of the projected unit cell area $d_{(100)\perp} \times d_{(001)\parallel}$ (Fig. 7e, black curve), which is compared to the expected projected area, calculated on the base of the simple Poisson model (the Poisson coefficient for LSCO film υ is about 0.3[34,35]). As is seen from the comparison of the black and red curves in Fig. 7e, the unit cell projected area should have been increased, however it is decreasing even below unstrained bulk value. In other words, the out-of-plane expansion is smaller than expected for the elastically compressed bulk, actually the material is even denser than the unstressed bulk. It can be understood if we assume that the oxygen vacancies ordering, which is known to expand the unit cell, accommodates part of out-of-plane stress. Ordering of oxygen vacancies in perovskites (and corresponding doubling of (001) parameter on HAADF images) is known as a Brownmillerite phase, which normally is not observed in Sr-doped LSCO at Sr substitution below 50%[18,19]. For LSCO/LAO sample, compressively strained in-plane, unidirection transformation to Brownmillerite phase can be promoted by out-of-plane lattice expansion.

The effect of the oxygen vacancy ordering is also present in the case of the LSCO film grown on the STO substrate. Figure 8a shows corresponding HAADF image. In this case, the substrate generates a tensile in-plane strain in LSCO layer and the lattice parameter doubling is observed in the direction along the

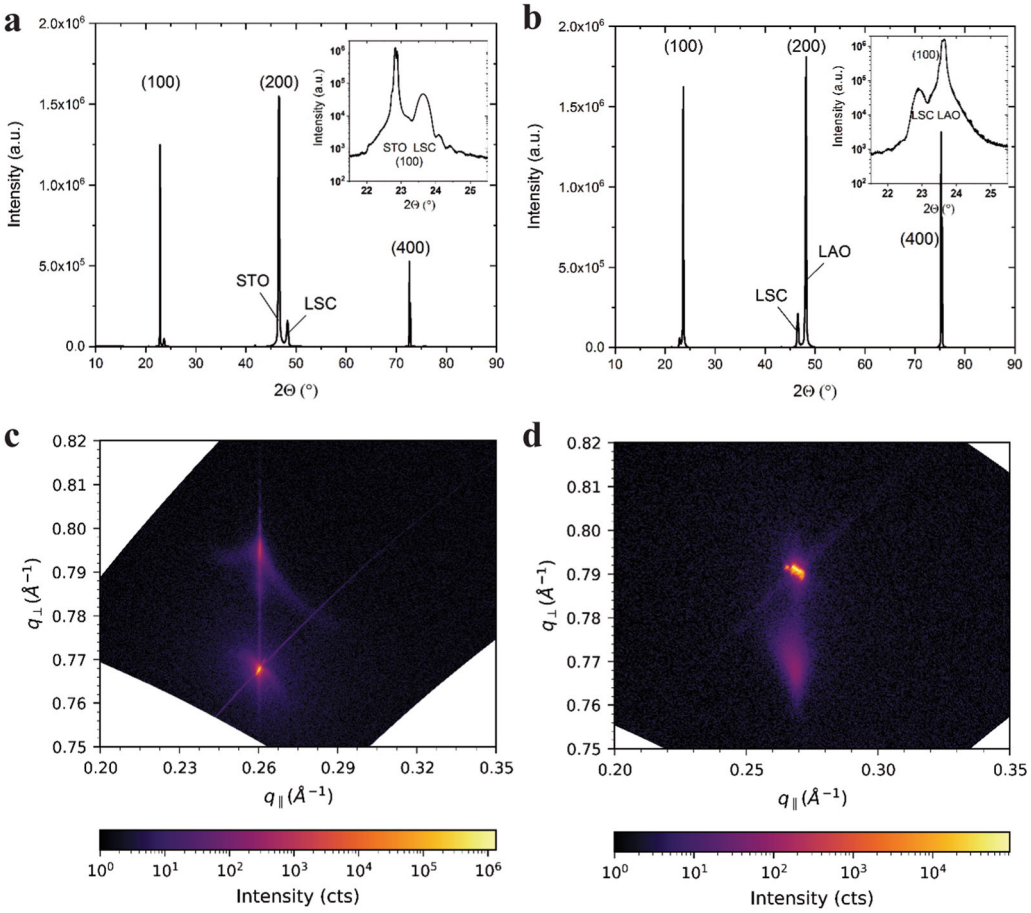

Fig. 6 X-ray diffraction in Bragg–Brentano geometry and X-ray reciprocal space mapping study. θ–2θ scans of **a** LSCO/STO and **b** LSCO/LAO show only {100} type diffraction peak of LSCO. The inset shows a magnification of the 001 peak. The good quality of the 20 nm epitaxial thin films is shown by the visible Kiessig fringes. X-ray diffraction reciprocal space maps are shown for **c** LSCO/STO and **d** LSCO/LAO thin films and demonstrate the in-plane lattice matching and out-of plain relaxation of LSCO. The substrate as well as thin film peaks are broader for LSCO/LAO.

interface. It is surprising, however, that in out-of-plane direction the parameter is also doubled, which can be attributed to the formation of Brownmillerite phase domains of different orientations. These out-of-plane domains compensate for the elastic compression perpendicular to the tensile stress, and thus average parameters in both directions do not deviate much from the unstrained bulk values (Fig. 8d).

GPA analysis shown in Fig. 8b–d clearly demonstrates the modulation of the lattice vector in two orthogonal directions in-plane and out-of-plane to the STO substrate. The average in-plane lattice parameter is 0.390 ± 0.007 nm and out-of-plane is 0.388 ± 0.007 nm. The projected unit cell area estimated from the Poisson model is shown in Fig. 8e in comparison with the one calculated directly from GPA analysis. Due to the mismatch with the STO substrate LSCO film expands in in-plane direction (the lattice parameter of the STO substrate is 0.3905 nm and unconstrained bulk LSCO is 0.387 nm) which should cause the constriction of the lattice vector in out-of-plane to the substrate and a total decrease of the unit cell volume of LSCO film is expected (estimated histogram of Fig. 7e). But as mentioned earlier the ordering of the oxygen vacancies tends to expand the lattice volume.

The strained state of the LSCO film grown on the STO substrate is maintained through its thickness (20 nm). For LSCO/LAO film the map in Fig. 7c indicates only slight relaxation the out-of-plane lattice parameter to the bulk value of LSCO towards the film surface.

In general, the LSCO system is known for its oxygen non-stoichiometry. Due to the substitution of La^{3+} by Sr^{2+} in bulk LSCO, the acceptor-type doping induces an increase in electron holes and also oxygen vacancies. A mix of both is created to neutralize the charge difference from Sr doping. In $La_{0.5}Sr_{0.5}CoO_{3-\delta}$ films, both grown in LAO and STO substrates, the appearance of strain-induced domain structure due to the ordering of the oxygen vacancies was demonstrated[18,19]. It is always accompanied by the occurrence of periodic dark stripes in Z-contrast STEM images similar to ones shown in Fig. 8. Additionally, it was observed that the orientation of the oxygen vacancy ordering in $La_{0.5}Sr_{0.5}CoO_{3-\delta}$ thin films depends on the substrate. In ref. [19], the authors showed that the oxygen-deficient planes in LSCO on STO are perpendicular to the substrate, whereas LSCO on LAO showed oxygen-deficient planes parallel to the substrate.

In order to confirm that the crystal structure is affected by the chemical composition changes, we performed energy-dispersive X-ray spectroscopy and electron energy loss spectroscopy (EELS) study of the O K and Co L23 edges for LSCO deposited on the STO and LAO substrates as shown in Supplementary Figs. 1 and 2. The compositional maps demonstrate atomically sharp interfaces in both cases. Also, the high spatial resolution is visible. The comparison of the selected spectra from different Co atomic rows did not show any significant difference for Co L23 edge in both cases. In contrast, the O K edge for Co1 type atomic rows in Brownmillerite phase shows a difference in comparison to the Co2 type atomic rows. This is in agreement with the previous

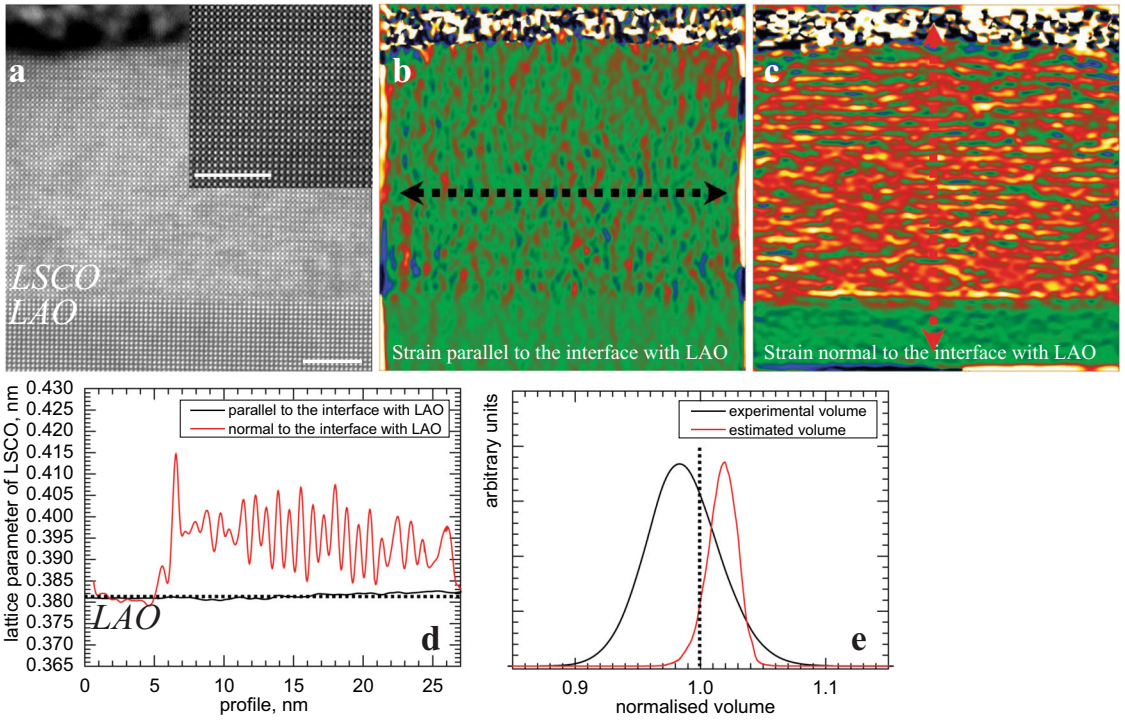

Fig. 7 Geometrical Phase Analysis of LSCO thin film grown on LAO(100) substrate. a HAADF STEM image, **b**, **c** strain mapping parallel and normal to the interface with the substrate, **d** profiles of the in-plane and out-of-plane lattice parameter corresponding to the dashed lines in **b** and **c**, **e** cell volume of the LSCO normalized to its bulk value measured and estimated by assuming a simple elastic model. The insert in **a** shows the magnified HAADF image. The scale bar is 5 nm.

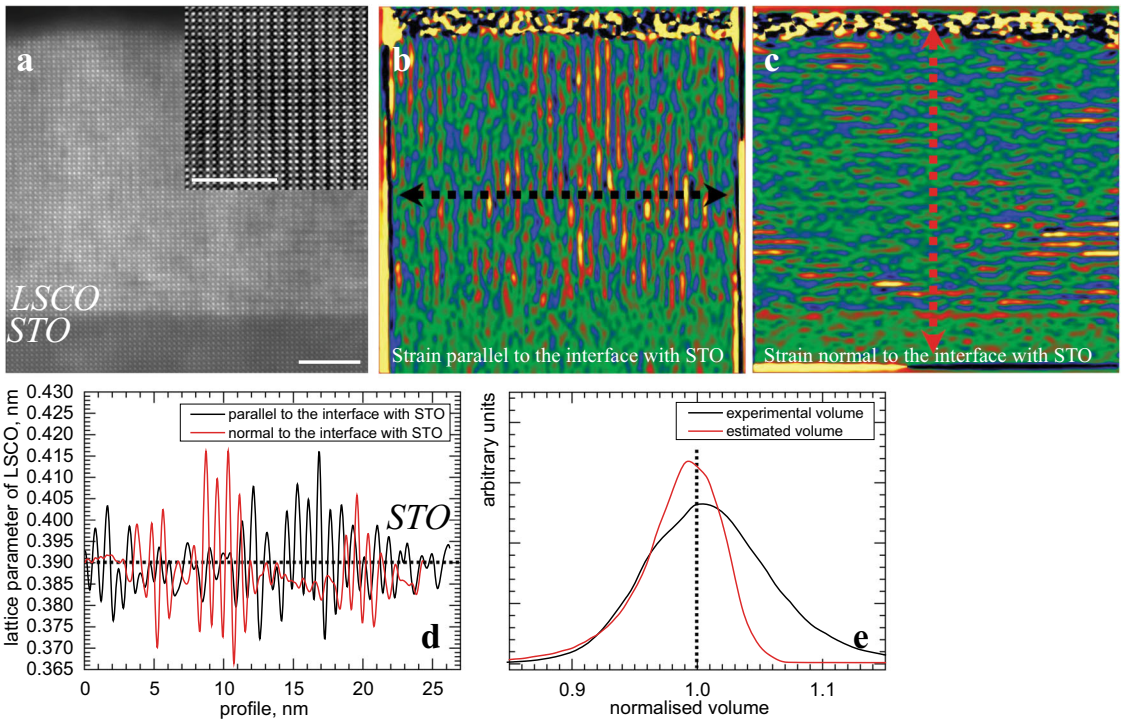

Fig. 8 Geometrical Phase Analysis of LSCO thin film grown on STO(100) substrate. a HAADF STEM image, **b**, **c** strain mapping parallel and normal to the interface with the substrate, **d** profiles of the in-plane and out-of-plane lattice parameter corresponding to the dashed lines in **b** and **c**, **e** cell volume of the LSCO normalized to its bulk value measured and estimated by assuming a simple elastic model. The insert in **a** shows the magnified HAADF image of the region with Brownmillerite phase schematically demonstrated in Fig. 1a. The scale bar is 5 nm.

study[18]. The fine structure of the O K edges from dark stripes on HAADF image (Co2 rows) reflects the slight decrease of oxygen content, although the analysis of the fine structure of the Co L23 edge does not show the change of the Co valence state. First-principles calculations provided an interpretation based on a model of nanometer-sized pockets with high-spin Co ions in the Co2 planes containing O vacancies, and low-spin Co ions in the Co1 planes[18]. There is no pronounced difference between O K edges collected from the different Co atomic rows for LSCO deposited on the LAO substrate.

We also utilized the recently introduced approach to calculate the coefficient of the oxygen nonstoichiometry δ based on the lattice vector change in perovskites[13]. The average δ measured from the GPA analysis is 0.05 for LCSO/LAO (taken into account the measured average out-of-plane lattice parameter 0.395 nm) and it is around 0.22 for LCSO/STO for Brownmillerite phase (taken into account the measured average lattice parameter for Co2 rows—0.416 nm). Similar estimations could be done from XRD data. Based on the data of δ in ref. [20], the δ is 0.04 for LCSO/LAO and 0.14 for STO/LAO. There is a good agreement with the TEM data especially taking into account the higher Sr concentration in LSCO film from ref. [20]. Relating these oxygen vacancy concentrations back to the isotope exchange measurements, we see that the difference is significantly smaller than the difference observed in tracer diffusion coefficient (a factor of 300). Consequently, it seems that both, the tracer concentration as well as mobility play a role for the different diffusion properties observed. Interestingly, not only directly lattice strain-related changes of the activation energy for migration but also vacancy association effects due to the high oxygen vacancy concentration have an important contribution.

The different structure of the LSCO thin films grown in tensile and compressive strain conditions was confirmed by HRTEM study. It is caused by the oxygen vacancies ordering affected by strain from the substrate. The pronounced domain structure of the Brownmillerite phase was found in tensile-strained LCSO grown on the STO substrate. It suggests significant local concentration of the oxygen vacancies with the average value of the oxygen non-stoichiometry of 0.22. In contrast, the lattice expansion due to the oxygen non-stoichiometry obtained for LSCO grown on the LAO substrate is significantly smaller. The simple Poisson model predicts even the larger volume expansion due to the mismatch with LAO substrate. The observed periodic modulation of the out-of-plane lattice parameter indicates the ordering of the oxygen vacancies to accommodate the epitaxial mismatch with the average value of the oxygen non-stoichiometry of 0.05. It agrees very well with our oxygen isotope exchange experiments. The tracer diffusion coefficient D^* and the tracer surface exchange parameter k^* have a huge difference depends on the strain state of the LSCO films. As the reason behind these differences, we assume a significantly changed oxygen vacancy formation enthalpy with mechanic strain and the Co spin state in accordance with literature[18]. So, the high spin state at the Co2 rows in the Brownmillerite phase could additionally contribute to the observed difference in the oxide ion diffusion kinetics. Moreover, the annealing could cause the improvement of the Brownmillerite phase ordering in tensile-strained STO increasing the D^*. Note that the oxygen vacancy ordering was found preferentially in planes parallel to the substrates in both cases, which may be responsible for the differences in the tracer diffusion measured in out-of-plane and in-plane geometry.

Methods

Sample preparation. $La_{0.6}Sr_{0.4}CoO_{3-\delta}$ powder was prepared via the nitrate/citrate (Pechini) route. The following high purity base materials were used: Co 99.995%, $SrCO_3$ 99.995%, La_2O_3 99.999%, HNO_3 70% in H_2O, 99.999% purity, citric acid monohydrate 99.9998% (all Sigma-Aldrich). A pulsed laser deposition target was produced by cold isostatic pressing (3.1 kbar, 1 min) and sintering (1250 °C, 12 h). Epitaxial $La_{0.6}Sr_{0.4}CoO_{3-\delta}$ thin films with ~20 nm thickness were prepared on 10 × 10 × 0.5 mm^3 $LaAlO_3$ and $SrTiO_3$ (100) single crystals (Crystec, Germany) by pulsed laser deposition. The target to substrate distance was 6.0 cm and the depositions were performed under 0.04 mbar O_2 pressure at 110 mJ/pulse laser energy, 1 Hz pulse frequency and 1000 total pulses.

Isotope exchange measurements. For isotope exchange measurements, Ti (10 nm) and Pt (100 nm) were sputtered as oxygen blocking layer on top of LSCO thin films on LAO and STO substrate, and then each single crystal was broken into four pieces ~5 × 5 × 0.5 mm^3 to assure minimal sample differences for subsequent isotope exchange experiments. Then, via photolithography and successive Ar^+ (3 kV, 1.8 mA, 40 min) ion beam etching, a 10 µm wide trench was etched through all layers (Pt, Ti, LSCO) and into the substrate, exposing 20 nm by 5 mm LSCO side surface on both sides of the trench which enabled oxygen exchange, compare ref. [36]. Oxygen isotope exchange experiments were then performed simultaneously for the thin films on LAO and STO in a special quartz setup. The samples were first heated to 680–780 °C in air (12 K/min, 1 h) to equilibrate LSCO. Then the samples were moved to a cool zone with a linear drive, and after cooling the atmosphere was changed by evacuating and refilling to 200 mbar 97.1% ^{18}O isotope enriched O_2 (Campro Scientific). Then the samples were reinserted into the hot zone and kept there for 1 h for the isotope exchange at 680–780 °C. Finally, the samples were cooled to room temperature at 60 K min^{-1} to freeze their tracer diffusion profiles. A pre-annealing in oxygen often reported in the literature was avoided as ^{18}O concentrations used here were above the natural abundance in bottled oxygen[37].

The resulting isotope diffusion profiles were subsequently measured by 3D profiling with ToF-SIMS (TOF.SIMS 5, ION-TOF) using 25 kV Bi+ primary ions in CBA measurement mode[38,39]. Negative secondary ions were analyzed in areas of 100 × 100 μm^2 up to 300 × 300 μm^2 using a raster of 1024 × 1024 measured points. For depth-profiling, 2 kV Cs^+ ions (300 × 300 or 500 × 500 μm^2, ca. 130 nA) were used for sequential ablation of the surface between measuring mass spectra. For charge compensation, a low energy electron flood gun (21 V) was used. In the recorded data, the LSCO layer was easily identifiable by monitoring the secondary ion signals of either Co^-, CoO^-, or CoO_2^-. The Poisson corrected oxygen isotope secondary ion counts of $^{16}O^-$ and $^{18}O^-$ of the LSCO layer were measured and analyzed.

X-ray diffraction. X-ray diffraction (XRD) in Bragg–Brentano geometry and X-ray reciprocal space mapping (RSM) were performed on LSCO thin films deposited on LAO and STO. Cu K_α X-ray sources emitting radiation with a wavelength of 1.5406 Å were used for all X-ray experiments. Reciprocal space maps were recorded by an Empyrean PANalytical Diffractometer with a GaliPix30Fass detector (both Malvern Panalytical Ltd.) between $\omega = 16.0–24.0°$ and $2\Theta = 70.0–91.4°$ for LSCO deposited on LAO, respectively; $\omega = 16.6–24.6°$ and $2\Theta = 76.5–90.5°$ for LSCO on STO. The Θ–2Θ XRD diffraction patterns were received using a PANalytical MPD Pro diffractometer equipped with a X'Celearator semiconductor detector (both Malvern Panalytical Ltd.) and a spinning stage. All diffractograms in Bragg–Brentano geometry were recorded between $2\Theta = 10–90°$.

Transmission electron microscopy. Electron microscopy studies were carried out with a transmission electron microscope (TEM), Titan G2 60–300 (FEI, Netherlands), equipped with a high-brightness field-emission gun (X-FEG). A dual beam (ion beam and electron beam) system (FEI Helios 450) was employed to fabricate the cross-sections of the samples. The electron energy loss spectroscopy (EELS) experiments were performed with a post-column high-resolution electron energy loss spectrometer (Quantum GIF Gatan) at 300 kV. The optical conditions of the microscope for EELS imaging and spectroscopy in STEM mode were defined to obtain a probe-size of 0.14 nm, with a convergence semi-angle of 10 mrad, and collection semi-angle of 12 mrad. High angle annual dark field (HAADF) STEM images for strain analysis were acquired in a fast sequence, aligned and summed up. This allowed neglecting global scan distortions due to the drift and average out local scan distortions due to vibrations and external magnetic field. Magnification was calibrated to the bulk lattice parameter of STO and LAO for the corresponding samples. Geometrical Phase Analysis (GPA) was performed using custom scripts[29].

Data availability

All data generated or analyzed during this study are included in the published article and the Supplementary Information, and are available from the corresponding authors upon reasonable request. Geometrical Phase Analysis (GPA) was performed using custom scripts available via https://www.researchgate.net/publication/225617264_Application_of_high-resolution_electron_microscopy_for_visualization_and_quantitative_analysis_of_strain_-fields_in_heterostructures.

Received: 10 January 2020; Accepted: 6 April 2020;
Published online: 08 May 2020

References

1. Steele, B. C. H. & Heinzel, A. Materials for fuel-cell technologies. *Nature* **414**, 345–352 (2001).
2. Jacobson, A. J. Materials for solid oxide fuel cells. *Chem. Mater.* **22**, 660–674 (2009).
3. Gao, Z., Mogni, L. V., Miller, E. C., Railsback, J. G. & Barnett, S. A. A perspective on low-temperature solid oxide fuel cells. *Energy Environ. Sci.* **9**, 1602–1644 (2016).
4. Peters, C., Weber, A. & Ivers-Tiffee, E. Nanoscaled $(La_{(0.5)}Sr_{(0.5)})CoO_{(3\text{-delta})}$ thin film cathodes for SOFC application at 500 °C < T < 700 °C. *J. Electrochem. Soc.* **155**, B730–B737 (2008).
5. Hayd, J., Dieterle, L., Guntow, U., Gerthsen, D. & Ivers-Tiffee, E. Nanoscaled $La_{0.6}Sr_{0.4}CoO_{3\text{-delta}}$ as intermediate temperature solid oxide fuel cell cathode: microstructure and electrochemical performance. *J. Power Sources* **196**, 7263–7270 (2011).
6. Ma, W. et al. Vertically aligned nanocomposite $La_{0.8}Sr_{0.2}CoO_3/(La_{0.5}Sr_{0.5})2CoO_4$ cathodes—electronic structure, surface chemistry and oxygen reduction kinetics. *J. Mater. Chem. A* **3**, 207–219 (2015).
7. Navickas, E. et al. Dislocations accelerate oxygen ion diffusion in $La_{0.8}Sr_{0.2}MnO_3$ epitaxial thin films. *ACS Nano* **11**, 11475–11487 (2017).
8. Adepalli, K. K., Yang, J., Maier, J., Tuller, H. L. & Yildiz, B. Tunable oxygen diffusion and electronic conduction in $SrTiO_3$ by dislocation-induced space charge fields. *Adv. Funct. Mater.* **27**, 1700243 (2017).
9. Kubicek, M. et al. Tensile lattice strain accelerates oxygen surface exchange and diffusion in $La_{1-x}Sr_xCoO_{3-\delta}$ thin films. *ACS Nano* **7**, 3276–3286 (2013).
10. Lee, D. et al. Stretching epitaxial $La_{0.6}Sr_{0.4}CoO_{3-\delta}$ for fast oxygen reduction. *J. Phys. Chem. C* **121**, 25651–25658 (2017).
11. Yildiz, B. "Stretching" the energy landscape of oxides—effects on electrocatalysis and diffusion. *MRS Bull.* **39**, 147–156 (2014).
12. Chen, X., Yu, J. & Adler, S. B. Thermal and chemical expansion of Sr-doped lanthanum cobalt oxide $(La_{1-x}Sr_xCoO_{3-\delta})$. *Chem. Mater.* **17**, 4537–4546 (2005).
13. Kim, Y.-M. et al. Probing oxygen vacancy concentration and homogeneity in solid-oxide fuel-cell cathode materials on the subunit-cell level. *Nat. Mater.* **11**, 888–894 (2012).
14. Zhang, N. et al. Oxygen vacancy ordering modulation of magnetic anisotropy in strained $LaCoO_{3-x}$ thin films. *ACS Appl. Mater. Interfaces* **10**, 38230–38238 (2018).
15. Zhu, L. et al. Strain-inhibited electromigration of oxygen vacancies in $LaCoO_3$. *ACS Appl. Mater. Interfaces* **11**, 36800–36806 (2019).
16. Yang, H. W. et al. Anomalous magnetism in strained $La_{1-x}Sr_xCoO_3$ epitaxial films $(0 \le x \le 0.5)$. *Sci. Rep.* **4**, 6206 (2014).
17. Torija, M. A. et al. Chemically driven nanoscopic magnetic phase separation at the $SrTiO_3(001)/La_{1-x}Sr_xCoO_3$ interface. *Adv. Mater.* **23**, 2711–2715 (2011).
18. Gazquez, J. et al. Atomic-resolution imaging of spin-state superlattices in nanopockets within cobaltite thin films. *Nano Lett.* **11**, 973–976 (2011).
19. Gazquez, J. et al. Lattice mismatch accommodation via oxygen vacancy ordering in epitaxial $La_{0.5}Sr_{0.5}CoO_{3-\delta}$ thin films. *APL Mater.* **1**, 012105 (2013).
20. Wu, X. et al. Glass-like through-plane thermal conductivity induced by oxygen vacancies in nanoscale epitaxial $La_{0.5}Sr_{0.5}CoO_{3-\delta}$. *Adv. Funct. Mater.* **27**, 1704233 (2017).
21. Han, J. W. & Yildiz, B. Enhanced one dimensional mobility of oxygen on strained $LaCoO_3(001)$ surface. *J. Mater. Chem.* **21**, 18983–18990 (2011).
22. Marrocchelli, D., Sun, L. & Yildiz, B. Dislocations in $SrTiO_3$: easy to reduce but not so fast for oxygen transport. *J. Am. Chem. Soc.* **137**, 4735–4748 (2015).
23. Metlenko, V. et al. Do dislocations act as atomic autobahns for oxygen in the perovskite oxide $SrTiO_3$? *Nanoscale* **6**, 12864–12876 (2014).
24. CrankJ. *The Mathematics of Diffusion*. 2nd edn, Oxford University Press: Oxford, 1979.
25. De Souza, R. A. & Kilner, J. A. Oxygen transport in $La_{1-x}Sr_xMn_{1-y}CoyO_{3\pm\delta}$ perovskites. Part I. Oxygen tracer diffusion. *Solid State Ion.* **106**, 175–187 (1998).
26. Kubicek, M., Limbeck, A., Fromling, T., Hutter, H. & Fleig, J. Relationship between cation segregation and the electrochemical oxygen reduction kinetics of $La_{0.6}Sr_{0.4}CoO_{3-\delta}$ thin film electrodes. *J. Electrochem. Soc.* **158**, B727–B734 (2011).
27. Marrocchelli, D., Sun, L. & Yildiz, B. Dislocations in $SrTiO_3$: easy to reduce but not so fast for oxygen transport. *J. Am. Chem. Soc.* **137**, 4735–4748 (2015).
28. Harrington, G. F. et al. The interplay and impact of strain and defect association on the conductivity of rare-earth substituted ceria. *Acta Mater.* **166**, 447–458 (2019).
29. Gutakovskii, A. K., Chuvilin, A. L. & Song, S. A. Application of high-resolution electron microscopy for visualization and quantitative analysis of strain fields in heterostructures. *Bull. Russ. Acad. Sci.: Phys.* **71**, 1426–1432 (2007).
30. Lim, J. & Yu, J. Role of oxygen vacancy in the spin-state change and magnetic ordering in $SrCoO_{3-\delta}$. *Phys. Rev. B* **98**, 085106 (2018).
31. Song, J. et al. Strong anisotropy and its electric tuning for brownmillerite $SrCoO_{2.5}$ films with different crystal orientations. *Phys. Rev. Mater.* **3**, 045801 (2019).
32. Shaibo, J., Zhang, Q. Y., Yang, R. & Guo, X. Ordering of oxygen vacancies in $LaBaCo_2O_{6-\delta}$ epitaxial films. *Scr. Mater.* **181**, 1–5 (2020).
33. Huang, H. et al. Topotactic transition between perovskite and brownmillerite phases for epitaxial $LaCoO_{3-\delta}$ films and effects thus resulted. *J. Phys. D: Appl. Phys.* **53**, 155003 (2020).
34. Alpay, S. P. et al. Effect of the electrode layer on the polydomain structure of epitaxial $PbZr_{0.2}Ti_{0.8}O_3$ thin films. *J. Appl. Phys.* **85**, 3271–3277 (1999).
35. Yu, X. et al. Pulsed laser deposition and characterization of heteroepitaxial $LiMn_2O_4/La_{0.5}Sr_{0.5}CoO_3$ bilayer thin films as model lithium ion battery cathodes. *ACS Appl. Nano Mater.* **1**, 642–653 (2018).
36. Zapata, J., Burriel, M., Garcia, P., Kilner, J. A. & Santiso, J. Anisotropic ^{18}O tracer diffusion in epitaxial films of $GdBaCo_2O_{5+\delta}$ cathode material with different orientations. *J. Mater. Chem. A* **1**, 7408–7414 (2013).
37. De Souza, R. A. & Chater, R. J. Oxygen exchange and diffusion measurements: the importance of extracting the correct initial and boundary conditions. *Solid State Ion.* **176**, 1915–1920 (2005).
38. Holzlechner, G., Kubicek, M., Hutter, H. & Fleig, J. A novel ToF-SIMS operation mode for improved accuracy and lateral resolution of oxygen isotope measurements on oxides. *J. Anal. At. Spectrom.* **28**, 1080–1089 (2013).
39. Kubicek, M. et al. A novel ToF-SIMS operation mode for sub 100 nm lateral resolution: application and performance. *Appl. Surf. Sci.* **289**, 407–416 (2014).
40. Kubicek, M. et al. Electrochemical properties of $la_{0.6}Sr_{0.4}CoO_{3-\delta}$ thin films investigated by complementary impedance spectroscopy and isotope exchange depth profiling. *Solid State Ion.* **256**, 38–44 (2014).
41. Berenov, A. V., Atkinson, A., Kilner, J. A., Bucher, E. & Sitte, W. Oxygen tracer diffusion and surface exchange kinetics in $La_{0.6}Sr_{0.4}CoO_{3-\delta}$. *Solid State Ion.* **181**, 819–826 (2010).

Acknowledgements

The authors kindly acknowledge the financial support by the Austrian Science Fund (FWF; No. P29148-N36).

Author contributions

M.K. produced the LSCO films and performed the isotope exchange measurements. Y.P.I. and A.C. performed the TEM investigations. M.S. and A.V. performed XRD–RSM study. Y.P.I., A.C., and M.K. performed data analysis and wrote the manuscript. H.H., J.F., and Z.L.Z. supervised the project. All the authors read the manuscript.

Competing interests

The authors declare no competing interests.

Additional information

Supplementary information is available for this paper at https://doi.org/10.1038/s43246-020-0027-0.

Correspondence and requests for materials should be addressed to Y.P.I.

Reprints and permission information is available at http://www.nature.com/reprints

Publisher's note Springer Nature remains neutral with regard to jurisdictional claims in published maps and institutional affiliations.